Delft University of Technology

Beam Waist Properties of Spiral Antenna Coupled HEB Mixers at Supra-THz Frequencies

Gaspar Silva, Jose Rui; Finkel, Matvey; Laauwen, Wouter M.; Yates, Stephen J.C.; Mirzaei, Behnam; Vercruyssen, Nathan; Young, Abram; Walker, Christopher; Gao, Jian Rong; More Authors

Important note
To cite this publication, please use the final published version (if applicable).
Please check the document version above.

Beam Waist Properties of Spiral Antenna Coupled HEB Mixers at Supra-THz Frequencies

José Rui Gaspar Silva , Matvey Finkel, Wouter M. Laauwen, Stephen J. C. Yates , Behnam Mirzaei , Nathan Vercruyssen, Abram Young, Craig Kulesa, Christopher Walker, Floris van der Tak, and Jian Rong Gao

Abstract—We have simulated and measured the beam properties of lens-antenna coupled hot electron bolometer mixers at a few supra-terahertz frequencies between 1.4 and 5.3 THz. The quasi-optical structures consist of an elliptical lens and a logarithmic spiral antenna. The model used for our simulations consists of a finite-element analysis to simulate the far-field radiation pattern of the antenna, geometrical optics to map the antenna radiation to the lens surface, and physical optics to calculate an arbitrary far field. We perform a thorough study of the beam properties, such as beam waist radius, phase center location and axial ratio by varying the diameter and extension of the lens, and misalignments of the antenna relative to the lens, at different operating frequencies. The simulation results are applied to the design and optimization of three different lenses for mixers to be operated at 1.4, 1.9, and 4.7 THz, respectively, which will be used in the heterodyne array receivers on board of NASA's balloon borne GUSTO observatory. The beam properties were verified experimentally by measuring the beam patterns in amplitude at multiple planes using a heterodyne technique. We found that the experimental results show good agreement with those from the simulations. Our work has delivered the mixers with the required beam characteristics for GUSTO.

Index Terms—Antenna arrays, antenna radiation pattern, cryogenic, lenses, terahertz (THz) radiation.

I. INTRODUCTION

HETERODYNE receivers at terahertz (THz) frequencies, between 0.1 and 6 THz, play an important role in astronomical observations because they provide an extremely high spectral resolution ($R\sim10^{6\text{-}7}$) [1]. This high spectral resolution is required to resolve atomic fine structure lines (e.g., [CII], [NII], [OI]), high-J lines of heavy molecules (e.g., CO) and ground-state lines of hydrides (e.g., H2O, HD) [1], that can only be found at THz frequencies. These lines are used in the study of chemical processes and dynamics of star-forming regions [2], [3], [4], [5]. Furthermore, they can also be used to image supermassive black holes [6] at a THz frequency using an interferometer because of their coherent nature. As the spatial resolution is diffraction limited and scales with frequency there is a need to develop receivers at higher frequencies, i.e., above 1 THz. Additionally, there is also interest in THz astronomic observatories based on an interferometer from space [7] instead of a single dish telescope which also improves the spatial resolution, and where heterodyne receivers are the key technology.

In a heterodyne receiver, a weak spectral signal from the sky is combined by a mixer element with a much stronger line signal from a local oscillator (LO). The mixer down converts the sky signal around the frequency of the LO into one at an intermediate frequency (IF) in the gigahertz range. The latter is fed into a spectrometer after amplification by a low-noise amplifier. At supra-THz frequencies, >1 THz, different mixer detectors can be used such as the superconducting magnesium diboride (MgB_2) [8] hot electron bolometer (HEB) or the niobium nitride (NbN) HEB [9], the latter being currently the most sensitive [1]. As LOs, solid-state sources based on multiplier chains are the choice below 2 THz [10], while quantum cascade lasers (QCLs) are the preferred sources above 2 THz [11], [12].

Besides, the noise performance of a mixer, its coupling scheme for the radiation from free space to the bolometer is also important. At THz frequencies, the coupling is realized using either a quasi-optical, lens-antenna, or feedhorn-waveguide scheme [1]. The feedhorn-waveguide, widely used at lower frequencies below 1 THz, has been implemented for receivers up to 4.7 THz. However, the reduced dimensions of the structures, required at higher frequencies, make manufacturing very challenging and expensive [13]. For the lens-antenna, demonstrated up to 5.3 THz [14], both lens and planar antenna are easily manufactured, making it a better option at supra-THz frequencies. A challenge in the application of a lens-antenna is the alignment of the antenna to the lens optical axis, which requires micrometer-level accuracy, which is not trivial due to the methodology required in this process [15].

At supra-THz frequencies, only two types of antennas, logarithmic spiral antenna [16], [17] and twin slot antenna [18],

José Rui Gaspar Silva and Floris van der Tak are with the SRON Netherlands Institute for Space Research, 9747 AD Groningen, The Netherlands, and also with the Kapteyn Astronomical Institute, University of Groningen, 9747 AD Groningen, The Netherlands (e-mail: j.r.g.d.silva@sron.nl; f.f.s.van.der.tak@sron.nl).

Matvey Finkel, Wouter M. Laauwen, and Stephen J. C. Yates are with the SRON Netherlands Institute for Space Research, 9747 AD Groningen, The Netherlands (e-mail: m.finkel@gmail.com; w.m.laauwen@sron.nl; s.yates@sron.nl).

Behnam Mirzaei, Nathan Vercruyssen, and Jian Rong Gao are with the SRON Netherlands Institute for Space Research, 9747 AD Groningen, The Netherlands, and also with the Optics Research Group, Imaging Physics Department, Delft University of Technology, 2628 CD Delft, The Netherlands (e-mail: b.mirzaei@tudelft.nl; nathan.vercruyssen@gmail.com; j.r.gao@sron.nl).

Abram Young, Craig Kulesa, and Christopher Walker are with the Steward Observatory, University of Arizona, Tucson, AZ 85721 USA (e-mail: young@physics.arizona.edu; ckulesa@arizona.edu; iras16293@gmail.com).

Color versions of one or more figures in this article are available at https://doi.org/10.1109/TTHZ.2022.3230742.

Digital Object Identifier 10.1109/TTHZ.2022.3230742

have been applied for quasi-optical HEB mixers. Until now, only the spiral antenna coupled HEB mixers have shown a high power coupling efficiency from the antenna to a bolometer and thus low noise performance up to 5.3 THz [9], [14], [19], while the twin slot antenna coupled HEB mixers have demonstrated good performance only up to 2.5 THz [20]. Furthermore, since the spiral antenna can work in such a wide frequency band, e.g., 1–6 THz, one common design can be applied to multiple receivers required for operation at different frequencies. This advantage can reduce the cost significantly. For the lens, we prefer an elliptical geometry since it has been found to provide both a high coupling of the radiation to an antenna and a higher Gaussicity of the beam compared with a hemispherical lens [21]. For these reasons, this combination was selected as the coupling scheme for the three heterodyne array receivers at 1.4, 1.9, and 4.7 THz on board of the NASA balloon borne GUSTO mission [22], [23].

To design lens-antenna systems that match well to the instrument optics we need to accurately predict their beam properties. In our case, the lens-antenna parameters of interest are the beam waist radius and phase center (waist location). These two parameters are key to define the beam propagation and beam coupling, which can be optimized in the lens-antenna design. We refer the reader to Fig. 19 of the work in [18] for a schematic of a Gaussian beam coupling to a lens-antenna as an example. The beam Gaussicity, which represents how close the beam is to the fundamental Gaussian mode, is also interesting. However, due to limitations of our experimental setup, it is out of the scope of this work. At supra-THz frequencies, these parameters are challenging to simulate since the lens dimensions considered are much larger than the wavelength. Therefore, it is difficult to fully simulate lens-antenna systems in finite-elements solvers due to the dense meshing required to obtain accurate results, of the order of a fraction of the wavelength.

Different lens-antenna combinations have been reported in the literature where the most extensive studies have been done for twin slot antenna based systems [18], [21], [24], [25], commonly operated around 1 THz or below. For lens-spiral antenna systems, several other studies exist [19], [26], [27]. All the studies earlier initially calculate the beam patterns produced by the antenna inside the lens using full-wave simulations. Then the equivalent electric and magnetic fields on the surface of the lens are used to derive the radiation pattern outside the lens using geometric optics (GO) and physical optics (PO). From all these studies, only the work in [19] simulated an integrated lens-spiral antenna in the frequency range up to 6 THz. In that work, the antenna impedance and radiation patterns were studied, but not the beam waist radius and phase center.

It is also challenging to experimentally characterize the beam propagation of an integrated lens-antenna system at supra-THz frequencies. While accurate phase and amplitude measurements have been performed at frequencies up to 1.6 THz [28], such measurements including the phase have never been reported at higher frequencies since it is difficult to phase lock the available LO sources. Nevertheless, beam patterns in amplitude have been measured at frequencies up to 5.3 THz [14], [19]. However, the measurements are limited to either an angular
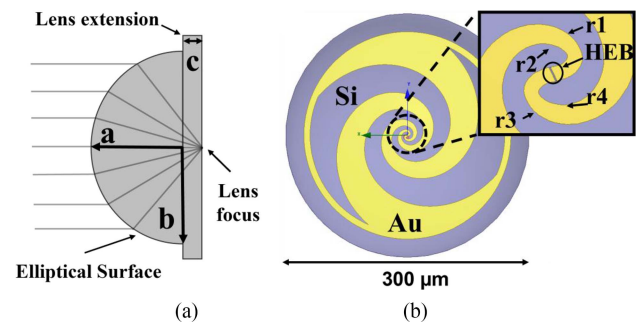

Fig. 1. Elliptical lens-spiral antenna design. (a) Schematic of the radiation of a collimated beam propagating from free space into the elliptical lens and being focused. For an ideal elliptical lens, the antenna location should match the second optical focus of the ellipse. (b) Structure of the simulated logarithmic spiral antenna, showing the HEB located in the center of its feed. The different arms are also labeled in the inset.

beam scan or a beam pattern mapped in a single plane. Although both measurements sufficiently characterize the far-field beam patterns, they are not sufficient to be able to determine the beam waist and phase center, which require measurements at multiple planes.

In this work, we report simulations and measurements of the beam properties of lens-antenna coupled HEB mixers at a few supra-THz frequencies between 1.4 and 5.3 THz. Our integrated lens-antenna structures consist of an elliptical lens and a logarithmic spiral antenna. Our goal is to study the beam properties of the integrated lens-antenna structures needed for an instrument, like GUSTO, such as the beam waist radius, phase center location, and beam axial ratio both theoretically and experimentally. The beam axial ratio is the ratio between the major and minor axis of the beam at the phase center location. Simulations and measurements regarding the beam waist radius and phase center location for lens-antenna have never been reported above 1.6 THz in the literature. A good understanding of these beam properties is crucial to obtain a good beam reproducibility, and therefore good uniform coupling, when developing arrays for an instrument such as GUSTO. We therefore perform tolerance sensitivity analysis for these parameters, which are critical for the proper manufacture of the lens-antenna mixer.

The rest of this article is organized as follows. In Section II, we start by introducing the lens-antenna design and the overview of how the simulations were performed. Section III describes the performed simulations, which are used in optimizing the lens-antenna designs for the three operating frequencies to meet the requirements of GUSTO. In Section IV, the experimental verification of the designs is shown using an amplitude-only heterodyne beam pattern technique, where the beams were mapped at multiple planes. Finally, Section V concludes this article.

II. SIMULATION MODEL

A. Lens-Antenna Design

Fig. 1 illustrates the lens-antenna design considered. In this system, a collimated beam propagating in free space is focused by the elliptical surface onto the ellipse second foci (the lens

focus) as shown in (a). The antenna is placed at the lens focus position and couples the radiation to the HEB detector, placed in the feed of the antenna, as highlighted in (b). The elliptical lens surface is defined by an ellipsoid hemisphere with a cylindrical extension. The ellipsoid surface is defined by the following equation:

$$\frac{x^2}{b^2} + \frac{y^2}{b^2} + \frac{z^2}{a^2} = 1, \ z \geq 0. \tag{1}$$

This surface is the equivalent of the elliptical surface shown in Fig. 1(a), a 2-D cross section, rotated symmetrically around the major axis of the ellipse "a." The major axis of the ellipsoid also coincides with the axis that is perpendicular to the plane of the spiral antenna. In this case, "b" represents the minor axis of the ellipse. The extension is added to the ellipsoid hemisphere to allow the placement of the antenna at the second focus of the ellipsoid. Such a lens can be designed by setting the minor axis "b," also referred as the lens radius in our case, that is perpendicular to the optical axis, and then calculating the major axis "a" using the following equation:

$$a = b\sqrt{\frac{\varepsilon_{Si}}{\varepsilon_{Si} - 1}} \tag{2}$$

where ε_{Si} is the dielectric constant of Silicon. Because the lens as a part of our mixer is operated at a liquid helium temperature, the ε_{Si} is 11.4 [29], which is slightly different from the value at room temperature.

To calculate the thickness of the cylindrical extension, which is referred as the extension length "c" and defines the location of the lens focus, which is the optimal location for the antenna, we use the following equation:

$$c = \sqrt{a^2 - b^2}. \tag{3}$$

The antenna consists of a two-arm widely wrapped logarithmic spiral as shown in Fig. 1(b), with each of the arms defined in (4a) and (4b) [27], with a starting radius $k = 4 \ \mu$m, curvature $a = 0.318$, and arm width $\delta = 83°$. These antenna parameters, or similar, have been used in the past, [9], [17] and are known to generate spiral antennas that cover a range between 1 and 6 THz. Furthermore, combining with an NbN bolometer located at the feed allows to achieve an impedance around 70 Ω that provides a good coupling between antenna and bolometer.

$$r1 = ke^{a\varphi}, \ r2 = ke^{a(\varphi - \delta)} \tag{4a}$$

$$r3 = ke^{a(\varphi - \pi)}, r4 = ke^{a(\varphi - \delta - \pi)}. \tag{4b}$$

B. Simulations

In our simulations, we use a very similar approach as in [27]. First, we do a finite-element analysis in HFSS [30] to simulate the antenna far field radiation pattern inside a lens. Due to the orientation of our antenna relative to the lens the polarization of interest is the left-hand circular polarization. Second, we use a hybrid approach of GO and PO to map the antenna radiation on the lens surface and calculate the far-field radiation pattern. More details on the HFSS simulations, GO and PO approach can be found in Appendix A.

III. TOLERANCE SENSITIVITY SIMULATIONS

We focus on investigating the effect of three different parameters: first, lens diameter; second, deviations from the nominal extension of the lens, hereafter simply extension deviations; and third, antenna misalignments relative to the lens; on key beam properties, such as beam waist radius, phase center and axial ratio of the output beam of the integrated lens-antenna system at different operating frequencies. The lens diameter is important because the lens design starts by defining this parameter, as described in Section II.A. The extension deviations are interesting to study because in reality, it is impossible to manufacture an ideal lens due to machining tolerances. Furthermore, this parameter has also been shown in the literature to change the beam divergence [27], which can potentially be used as a beam-tuning parameter. Lens-antenna systems are difficult to assemble, due to possible misalignment between the antenna and the lens. This misalignment not only affects the beam parameters but also creates undesired beam steering, which represents a deviation of direction of propagation of the beam relative to the ideal assembly case. Beam steering can reduce the coupling efficiency of the mixer to the desired optical system. Another interesting parameter is the shape error of the lens. However, this is not an issue since even at the highest frequency, the wavelength is still considerably larger than the standard manufacturing tolerances, e.g., at 5.3 THz the tolerances are below 0.1 μm [31]. With these simulations, we are able to understand how to design a lens-antenna system in the supra-THz, which can optimally match the desired optical requirements of GUSTO. The beam waist radius has a requirement of 4.0 ± 0.2 mm for Band 1 (B1) at 1.4 THz, 3.8 ± 0.2 mm for Band 2 (B2) at 1.9 THz and 1.8 ± 0.2 mm for Band 3 (B3) at 4.7 THz. For the phase center, the requirement was a maximum phase center position difference between the lenses, and between a lens and the array, smaller than the confocal distance, Z_c, see (B.2b) in Appendix B. Since the instrument can be refocused, the latter requirement ensures that the coupling loss due to phase center mismatch between the instrument and each pixel is acceptable. The methodology used for obtaining the beam waist radius w_0 and phase center Z_0 for each lens parameters can be found in Appendix B.

A. Beam Pattern Versus Lens Diameter

We start by studying the ideal elliptical lens geometry, where the antenna is located at the ellipsoid focus, for 5- and 10-mm lens diameters. In this geometry, the nominal extension length is 1550 μm for the 10 mm lens and 775 μm for the 5 mm lens. In Fig. 2(a), we present the far-field beam pattern in the plane that is 2500 mm away from the lens for the 10 mm diameter lens, operated at 1.4 THz. The beam is elliptical with the side lobes being nonuniform and localized across the beam minor axis, indicated by the dashed line in black. We observe a rotation of the elliptical beam orientation as a function of the operating frequency, with an angle between the horizontal axis and the beam major axis being 48°, 100°, 155°, 264°, and 277°, at 1.4, 1.9, 2.5, 4.7, and 5.3 THz, respectively. The observed rotation agrees well with the predicted angles versus frequency using formula (8) of the work in [16]. The beam ellipticity and
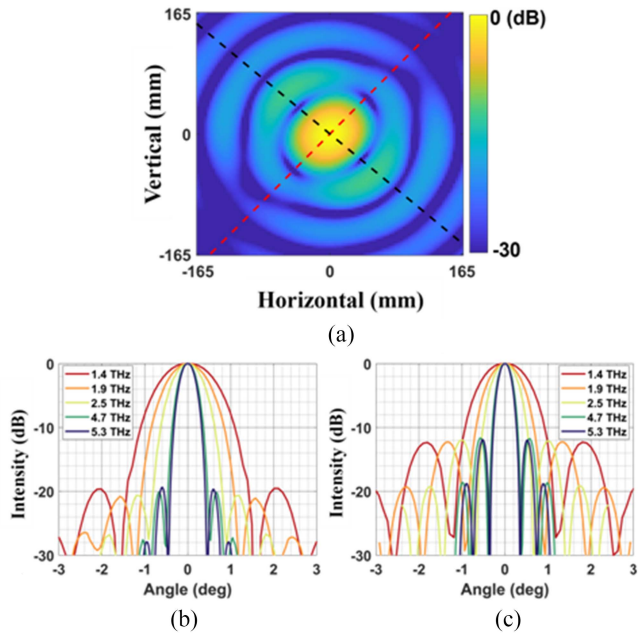
Fig. 2. Calculated far-field beam patterns for an ideal 10 mm elliptical lens. (a) 2-D beam pattern calculated at 1.4 THz and at a distance from the lens, Z = 2500 mm. The beam is elliptical and has nonuniform sidelobes. (b) and (c) Cross section of the far-field beam patterns at different frequencies along (b) minor and (c) major axes as indicated in (a).
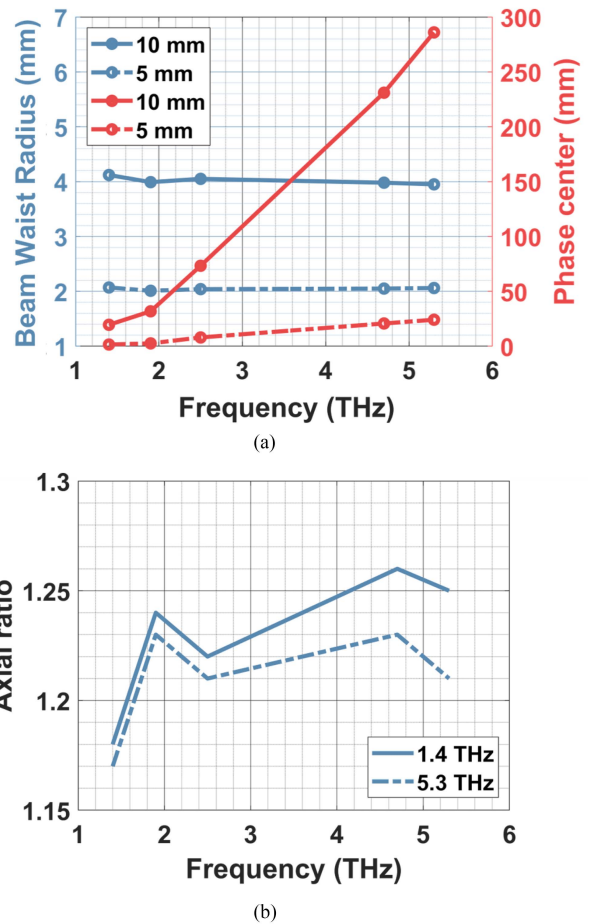

Fig. 3. Simulation results of the beam properties for the 10 mm lens as well as a 5 mm lens. (a) Beam waist radius and phase center, (b) axial ratio, as function of the frequency.

orientation dependence on the frequency are due to the use of the spiral antenna. In these antennas the active region changes as a function of the frequency [19], causing the beam rotation. The beam ellipticity is caused by the antenna geometry that generates an elliptical field. This ellipticity can be controlled by changing the parameter δ, with higher values leading to less elliptical beams [26]. Due to the beam ellipticity the analysis of the beam propagation results in different phase center locations, Z_{0x} and Z_{0y}, but also different beam waist radius, w_{0x} and w_{0y}. For simplification, throughout this work, we consider both orthogonal directions to have the same Z_0 and w_0. More details on the validity of this simplification can be found in Appendix B.

Fig. 2(b) and (c) plot the cross section of the far-field beams along the minor and major axis, respectively, for the 10 mm lens and at five different frequencies. The beam becomes more collimated when the frequency increases, as expected for a diffraction-limited system given the lens size. For the cross-section plot along the minor axis the sidelobe level is -13 dB, while along the major axis it ranges between -22 and -20 dB. The beams calculated for the 5 mm lens show a similar behavior to the 10 mm lens and are therefore not shown.

Fig. 3(a) and (b) summarize the beam properties versus frequency for both lens diameters. The beam waist radius is found to depend on the lens diameter, but not on the frequency, and to be approximately 80% of the respective lens radius, e.g., for the 10 mm diameter lens the beam waist radius is 4.1 mm. In addition, this result implies that smaller diameter lenses have more divergent beams as expected in [18] and [27]. The phase center moves further away from the lens as the frequency increases, where at 5.3 THz a 10 mm lens has the phase center 290 mm in front of the lens. Nevertheless, we note that for a 10 mm lens

the Z_C, ranging from $\sim$250 mm at 1.4 THz to $\sim$840 mm at 5.3 THz, is considerably larger than the observed phase center displacements. The phase center displacement versus frequency is an expected property of the spiral antenna [32]. The axial ratio increases marginally at higher frequencies.

B. Beam Pattern Versus Lens Extension Deviations

Fig. 4 summarizes the cross sections of the far-field beams along the major and minor axis for the 10 mm diameter lens with an extension of 1535 μm in (a) and (b), respectively, which has a -15 μm deviation relative to the nominal extension, and 1565 μm in (c) and (d), respectively, which has a $+15$ μm deviation. The simulations are performed at five frequencies. The beam deformation is clearly visible by comparing the differences in the beam profile relative to the previous results from the lens with the nominal extension in Fig. 2.

To better understand the impact of the extension deviations on the beam properties, we now investigate a wide range of extensions for the 10 mm lens. We consider a range between 1470 to 1630 μm with a 5 μm step, representing a ±80 μm extension variation from the nominal extension, at the two extreme frequencies, 1.4 and 5.3 THz. Fig. 5 summarizes the calculated
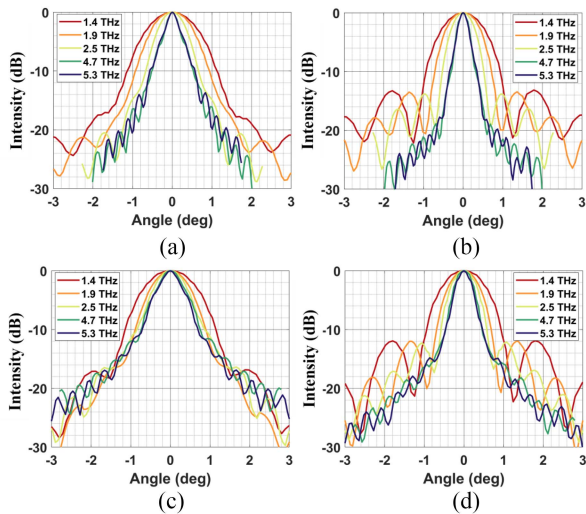
Fig. 4. (a) Far-field simulations results for 10 mm lens diameter with nonideal extension versus frequency. (a) and (b) Beam profile overview for a lens with 1535 μm extension, across the beam major and minor axis, respectively. (c) and (d) Beam profile overview for a lens with 1565 μm extension across the beam major and minor axis, respectively. The nominal extension of the lens is 1550 μm.
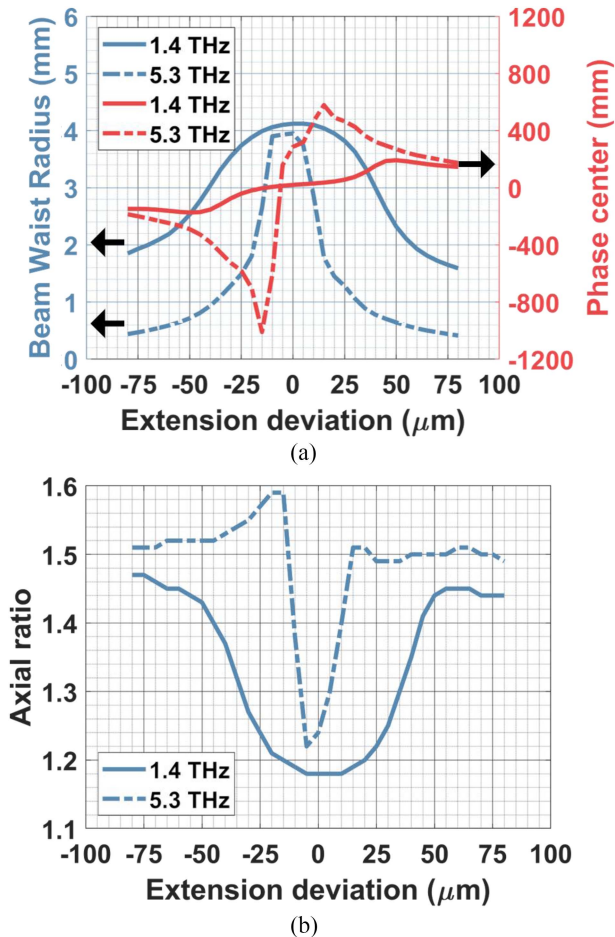

Fig. 5. Simulation results of the beam properties for a 10 mm diameter, elliptical lens by varying its extension deviation, at 1.4 and 5.3 THz. The nominal extension of the lens is 1550 μm. Calculated beam waist radius and phase center in (a), and axial ratio (b) are plotted as a function of extension.

beam properties as a function of the extension deviation relative to the nominal extension (1550 μm). From these plots, overall, we see similar behavior at both 1.4 and 5.3 THz; however, the higher frequency always shows a stronger dependence.

The beam waist radius shows a bell-shaped curve, with the maximum centered at the zero-extension deviation. It is followed by a fast decrease in the waist size, implying an increase of the beam divergence. The significant drop starts at the $\pm$ 20 μm extension deviation at 1.4 THz and at $\pm$ 5 μm at 5.3 THz. The phase center relative to the lens peaks around the $\pm$ 15 μm extension deviation at 5.3 THz, and around $\pm$ 45 μm extension deviation at 1.4 THz. For context, the maximum Z_C for the simulated beams, which occurs for the largest beam waist, is 250 mm at 1.4 THz and $\approx$840 mm at 5.3 THz. The axial ratio follows the inverse behavior comparatively to the beam waist radius, where the axial ratio increases as the extension deviates further from the ideal, leading to more elliptical beams.

Our results, in particular the shape of the curves for the waist size and location, are similar to the ones observed in [27] for a spiral antenna.

C. Beam Pattern Versus Antenna Alignment Errors

We have simulated different misalignments between the antenna and the optical axis of an ideal elliptical lens with 10 mm diameter. In Fig. 6, we present the simulation results for 5, 10, and 30 μm misalignments in both the horizontal (a), (b), (c) and the vertical (d), (e), (f) direction at 5.3 THz. From these plots, we conclude that as the misalignment increases in either direction, the beam pattern is more affected. We observe the main lobe becoming less elliptical if the misalignment direction is closer to the minor axis direction, see (a), or more elliptical if the misalignment direction is closer to the major axis direction, see (b). There is also an asymmetry of the side lobe level along the beam axis closer to the orientation of the misalignment. The sidelobe asymmetry is visible in (c) and (e), for the horizontal and the vertical misalignment direction, respectively. This behavior agrees well with what was reported in [19] and [27]. On the other hand, for the beam axis closer to the orthogonal direction to the misalignment, the beam remains almost unaffected as visible in (b) and (f), for the horizontal and the vertical misalignment direction, respectively. Both behaviors seen for the main lobe and sidelobes are caused by the asymmetric illumination of the lens surface, causing the beam aberrations such as the asymmetry observed.

The beam parameters for the different misalignments are summarized in Fig. 7(a) and (b). Both beam waist radius and phase center are barely affected by the misalignment, where even with a 30 μm misalignment we observe less than 2% change in the waist size. The axial ratio changes depending on the orientation of the misalignment as indicated by the plots in Fig. 6. Here, the beam ellipticity can either increase or decrease depending on the direction of the misalignment. Despite of the fact that the misalignment might negatively affect the beam quality, we find that for the 5 μm misalignment cases the beam parameters are still very close to the perfect alignment case,
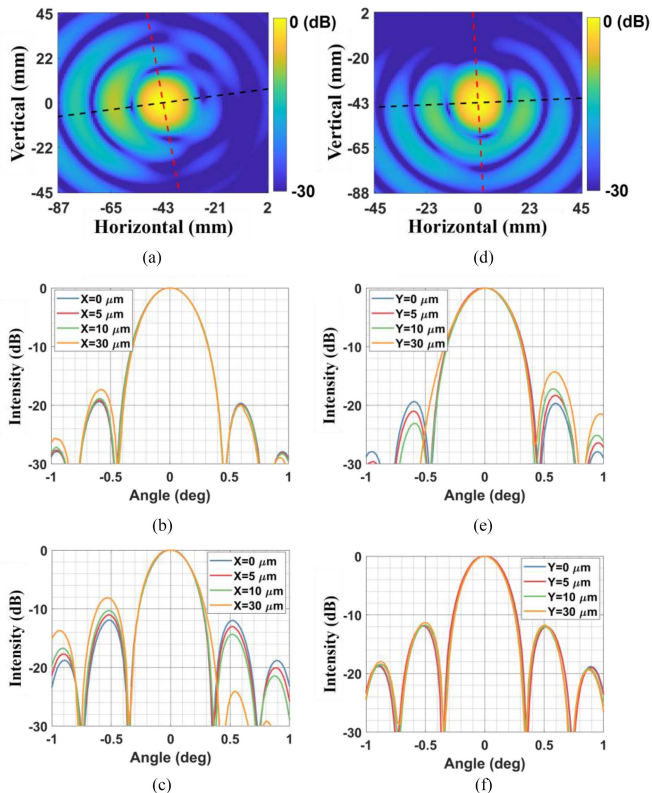
Fig. 6.   Simulated far field beams at 5.3 THz for different antenna misalignments relative to the optical axis of a 10 mm diameter lens. (a) Beam pattern calculated at Z = 2500 mm for a +30 μm horizontal offset. (b) and (c) Major and minor axis cross section, respectively, for the far-field beam patterns for different horizontal antenna misalignments. (d) Beam pattern calculated at Z = 2500 mm for a +30 μm vertical offset. (e) and (f) Major and minor axis cross sections, respectively, for the far-field beam patterns for different vertical antenna misalignments. For panels (b) to (f) the beam steering for each individual beam is not shown, with the 0° representing each beam boresight direction.
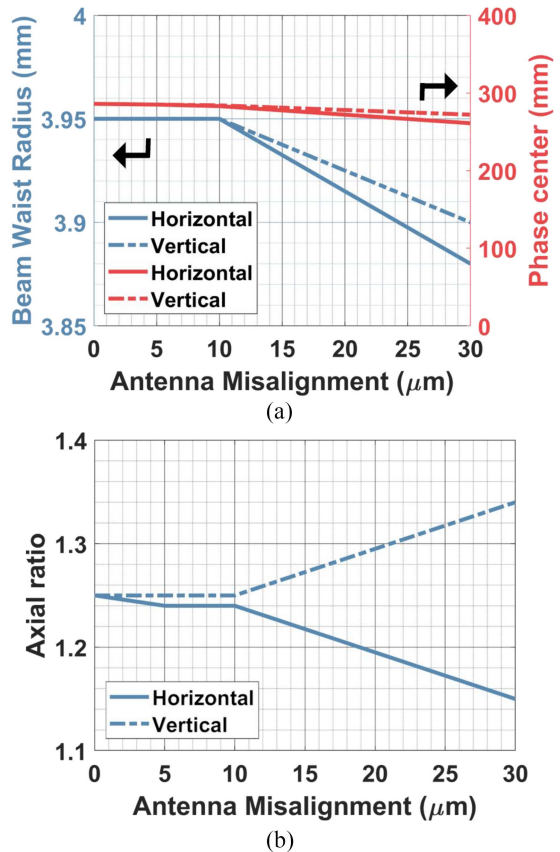

Fig. 7.   Simulation results of the beam properties for the simulations of different antenna misalignments at 5.3 THz. (a) Beam waist radius and phase center. (b) Axial ratio versus antenna misalignment.

TABLE I
LENS DESIGN PARAMETERS

Lens type	a (mm)	b (mm)	c[a] (μm)
B1	5.235	5.000	1542
B2	5.235	5.000	1527
B3	2.617	2.500	767

[a]The extension values include the detector chip, which has a Si substrate with a thickness of 342 ± 2 μm.

with a small sidelobe level asymmetry and also a small change in the axial ratio. We conclude that a 5 μm misalignment can be used as an upper limit for the misalignment for the 10 mm lens diameter at 5.3 THz. We do not discuss the results at the lower frequencies because the same misalignment causes a smaller effect on the beam properties. Lastly, we discuss the beam steering effect caused by the misalignments. For each misalignment case, this effect was calculated by fitting the slope of the beam displacement across multiple planes, from which we obtained the angle relative to the Z-axis. We then normalize the calculated angle relative to the total misalignment, obtaining a beam steering factor. For the six misalignment cases, we found a similar beam steering factor of 0.033°/μm for the 10 mm diameter lens. This value was also found to be consistent for different frequencies, with less than 1% difference between 1.4 and 5.3 THz for a 30 μm misalignment. Furthermore, simulating the beam steering for different lens diameters between 2 and 10 mm we found the general beam steering factor to follow the relationship 0.33/D deg/μm, where D is the lens diameter, within 1% error. The beam steering factors for both 10 and 5 mm lenses have been experimentally verified in a separate study, showing very good agreement with these simulations [33].

IV. EXPERIMENTS

A. Lens Design

Based on the GUSTO telescope requirements, see Section III, and the previous tolerance analysis we designed lenses with the dimensions presented in Table I.

B. Experimental Setup

Fig. 8 presents the detailed setup used in our experiments. The THz radiation used to probe the lens-antenna beam pattern originates from a glow bar, IR-Si207 source from Hawk Eye Technologies, assembled in a setup similar to the one used in [34]. This glow bar setup is mounted on a high precision XYZ stage, three-axis 8MT295 Series from Standa, that allows us to
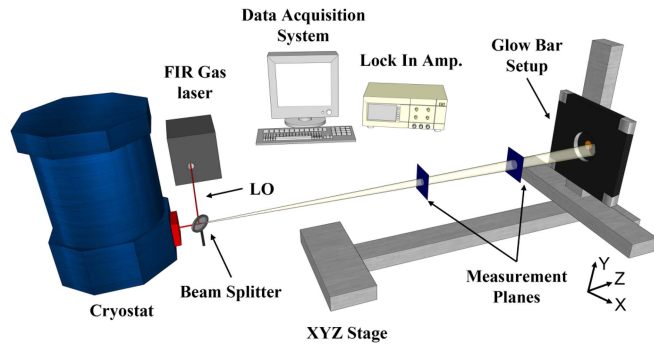
Fig. 8. Experimental setup. The mixer block is cooled to liquid helium temperature inside the cryostat. The radiation from the glow bar is combined with that of an LO originated from the FIR gas laser in the Mylar beam splitter and coupled into the cryostat. The mixer is operated in heterodyne detector mode by pumping the device to its optimal working point using a combination of dc bias and LO power, the latter tuned to the desired THz line. The glow bar source is chopped at a frequency of 38 Hz and scanned in front of the cryostat in different planes. The lock-in amplifier measures the ac response of the IF power.
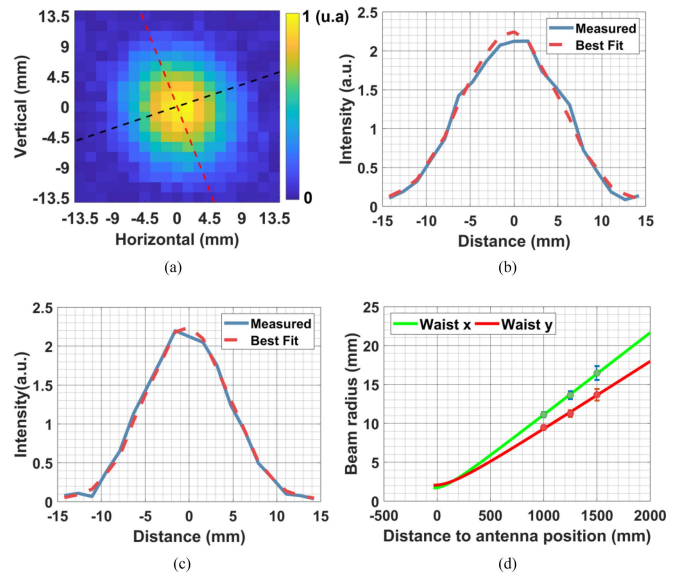

Fig. 9. Beam measurements at 5.3 THz for B3-D lens, the parameters of which are listed in Table I. (a) Measured beam pattern at a distance of 1000 mm away from the lens. (b) and (c) Major and minor axis cross sections, respectively, with measured and best fit profile, for the beam in (a). (d) Quasi-optical beam propagation fitting using linear least square fits.

scan the glow bar in front of the cryostat. The LO is a far-infrared (FIR) gas laser at the desired operation frequency. The radiation from the glow bar and the LO are combined in a 3 μm mylar beam splitter, with the combined radiation propagating through the optical path of the cryostat into the lens-antenna mixer. The cryostat optical path consists of a QMC 6 THz multimesh low-pass filter at 4 K and a UHMWPE window at 300 K. The lens-antenna mixer with an NbN bolometer located at the antenna's feed is mounted on a metal block, which is fixed on the 4.2 K cold plate of the IR liquid helium cryostat. The NbN bolometer is 2 μm in width, 0.15 μm in length and 5 nm in thickness, and is similar to the one used in [14].

The beam patterns are obtained by scanning the glow bar in the XY plane perpendicular to the optical axis of the cryostat, measuring the response of the HEB operated in heterodyne detector mode. The device is operated at the optimal dc bias and with the optimal LO power, which gives the best heterodyne sensitivity. The glow bar signal is chopped at a frequency of 38 Hz to allow the use of a lock-in amplifier (LIA) to acquire the IF output power of the HEB in ac, improving the signal-to-noise ratio (SNR) by reducing the sensitivity to dc drifts and hence 1/f noise in the setup. The IF chain consists of a bias-T and a cryogenic LNA, attached to the 4 K cold plate of the cryostat. The IF chain at room temperature includes two LNAs, a narrow band pass filter (BPF) and a diode power detector. The latter is acquired by the LIA. The BPF filter of the IF is at 1.5 GHz with a bandwidth of 80 MHz.

To obtain the beam parameters experimentally, we follow the same procedure as for the simulations. We measure beam patterns at different Z-axis positions. To each measured beam pattern, we fit an elliptical Gaussian using (B.1). However, in this case, we add a noise floor term to the equation. From the fitting, we obtain the beam radius dimensions, w_x and w_y for that particular plane. The beam radius dimensions from the different planes are then used to estimate the beam waist radius, w_0, and the beam phase center, Z_0, using (B.2a) in Appendix B.

C. Measurement Results

The designed lenses were verified experimentally at the intended frequency of operation except for the B3 lenses that were characterized and analyzed at 5.3 THz instead of 4.7 THz. The reasons for this are: the 4.7 THz radiation available from a QCL is not suitable for such a measurement because of strong water absorption; and 5.3 THz is the closest frequency line available from the FIR gas laser which suffers less absorption. For each measured beam, the first plane scanned and recorded is 900–1000 mm from the lens. This distance was chosen to guarantee that the measured beams are in the far-field limit and that there is a sufficiently high SNR for the measurements. For a particular experiment, the total number of planes scanned, at different Z-axis positions, ranges between 2 and 6 depending on the SNR.

Fig. 9 presents an example of the measurements for the B3-D lens, see Table II, with the HEB operated at 5.3 THz. Panel (a) shows the beam pattern at the first plane, 1000 mm away from the lens, with the major (red) and minor (black) axis orientation overlaid. (b) and (c) Show the respective axis cross sections of both the measured profile and best Gaussian fit. The plot in (d) shows the beam propagation fitting where the beam waist radius and phase center are derived. The average beam waist radius was found to be 1.9 ± 0.1 mm whereas in the simulations we expected 1.9 mm as well. The measured phase center is -40 ± 75 mm, while in the simulations it is at -30 mm. The measured axial ratio is 1.2 ± 0.1 whereas the simulated ratio is 1.20.

In Table II, we summarize the beam waist radius and phase center from both simulations and measurements for all the experiments. From the comparison between the simulated and measured results, we find that the beam waist radius is very

TABLE II
RESULTS OF THE AVERAGE BEAM WAIST RADIUS AND PHASE CENTER OF ALL
THE LENS-ANTENNA SYSTEMS OBTAINED FROM BOTH SIMULATIONS AND
MEASUREMENTS

Lens[a]	Freq (THz)	Simulations		Measurements	
		w_0 (mm)	Z_0 (mm)	w_0 (mm) ± 0.1 mm	Z_0 (mm) ± 75 mm
B1-A	1.4	4.1	10	4.0	−40
B2-A	1.9	3.6	−80	3.6	30
B3-A				1.9	−180
B3-B		1.9	−30	2.0	−150
B3-C	5.3			1.8	−10
B3-D				1.9	−40

[a]The lens parameters can be found in Table 1.

[b]w_0 is the beam waist radius and Z_0 is the phase center of the beam. See Appendix B for further details.

similar to the designed value. For B1-A lens at 1.4 THz the simulated beam waist radius is 4.1 mm whereas the measured value is 4.0 mm, being 3% lower. For B2-A at 1.9 THz both simulated and measured are the same and equal to 3.6 mm. For B3 at 5.3 THz, the simulated beam waist radius is 1.9 mm, while the measured value, averaged over the measurements for B3-A, B, C, and D, is also 1.9 mm. All the lenses meet the beam waist radius requirement for GUSTO. From the measured lenses we obtain a Z_C of 237 mm for B1, 260 mm for B2 and 195 mm for the averaged beam waist radius over the B3 lenses. In terms of the phase center, all are found close or behind the expected location except for the B2-A lens, where the phase center is found 110 mm in front of the expected value. Additionally, the largest difference between simulations and measurements for the phase center is for the B3 lenses, where a maximal difference of 150 mm is found for B3-A, which is larger than the error bar. We attribute the variations of the phase center to variability in the fabrication of these lenses as observed in [33] for the same and other lenses. Such fabrication errors can lead to large variations of the phase center while the waist radius remains almost unchanged, as observed for small extension deviations in Fig. 5. However, the Z_C is so large for all the measured lenses that we still meet the requirements for GUSTO. In particular for the B3 lenses, it is possible to place the instrument phase center such that it is within less than half the Z_C to each of the different lenses phase center, so that the coupling loss due to the phase center mismatch is acceptably low. The ± 0.1 error bar for the waist size was derived from the average fitting errors, while the ± 75 mm uncertainty for the phase center was obtained from propagating the waist size errors in the fitting of (B.2). The latter are considerably below the Z_C for all the lenses and therefore good enough to characterize this parameter.

The axial ratio measured for the B1-A lens was 1.2 ± 0.1 and the simulated 1.18. For the B2-A lens, we measured 1.2 ± 0.1 and the simulated 1.26. For the B3 lenses, we measured 1.2 ± 0.1 mm, for all four lens, whereas the simulated was 1.20. For all the B3 lenses we observe an axial ratio being the expected. For
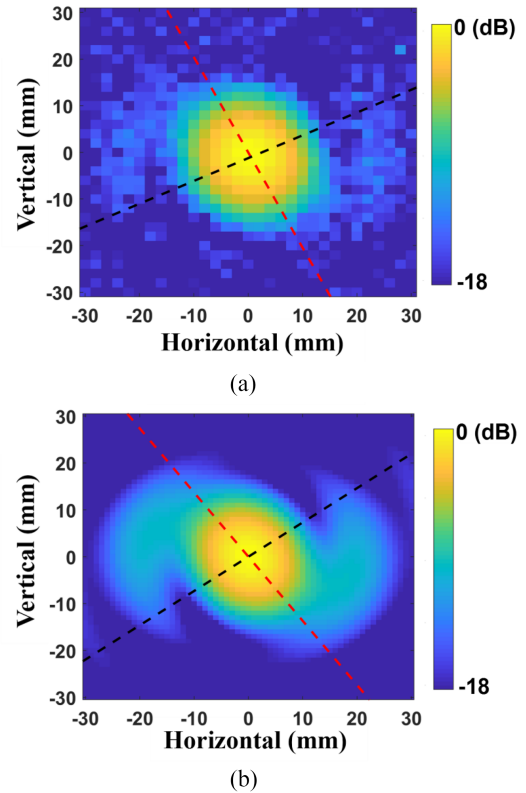

(a)

(b)

Fig. 10. (a) and (b) Measured and simulated beam patterns, respectively, at 1.9 THz at a plane that is 900 mm from the antenna for a 10 mm diameter lens with an extension of 1535 μm, representing a deviation of −15 μm from the ideal elliptical geometry.

the B1 and B2 lenses, there is a larger difference, in particular for the B2 lens, however, we note that in these experiments we have not corrected for the beam steering error, which was found, for similar lenses, to be potentially equivalent up to 30 μm misalignment between the antenna and the lens optical axis [33]. We believe such misalignment errors combined with the measurement uncertainty can explain the axial variations observed as shown in Section III.

D. Beam Pattern Analysis

The Gaussicity of the beams was not addressed because we do not have a sufficiently high SNR to map the sidelobes. A solution would be to perform considerably longer scans, however, the stability of the FIR gas laser prevents us to do so [35]. However, to have a qualitative understanding of the beam pattern we scanned the beam pattern over a larger area for the B2-A lens. This lens was chosen since it is expected to have a larger beam deformation from the three types of lenses. Fig. 10 shows both measured beam pattern in (a) and simulated one in (b). We observe good agreement on the beam orientation, the sidelobe shape, and location. The major axes of both beams, in red, have a difference of 7°. This angular difference can be explained by a rotation of the mixer relative to the metal block where it is assembled. In terms of the sidelobe level, the maximum in the measurement is ≈ -13 dB, whereas we obtained ≈ -10 dB in the simulations.
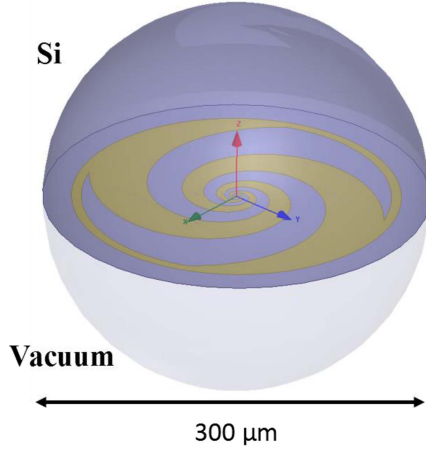
Fig. 11. Simulated antenna structure in HFSS. The spiral antenna is assumed to be patterned between two homogenous media, vacuum, and Silicon. We calculate the antenna's far-field radiation that propagates into the Si medium.
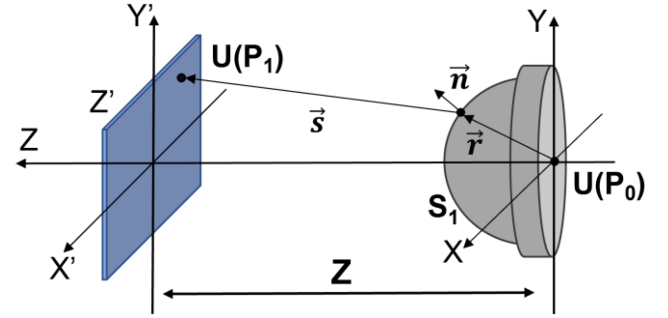

Fig. 12. Schematic of the electrical field propagation from the XY plane, where the antenna is located, to the x'y' plane, the far field plane of interest. $U(P_0)$ is obtained from the HFSS simulations.

V. CONCLUSION

We have performed beam simulations for THz HEB mixers using a combination of an elliptical lens with a logarithmic spiral antenna at a few supra-THz frequencies up to 5.3 THz. The model used combines a finite-element analysis in HFSS to simulate the far-field antenna radiation pattern with a PO approach to simulate the propagation of the radiation through the lens into an arbitrary far field plane in free space. We have studied the effect of the lens diameter, lens extension deviations, and misalignments between the antenna and the lens optical axis, on the beam properties of the integrated lens-antenna structures, such as beam waist size, phase center, and beam axial ratio.

Three different lenses, B1, B2, and B3, were optimized for the heterodyne instrument onboard NASA's upcoming GUSTO observatory. The beam waist radius and phase center were measured at 1.4 THz for B1, 1.9 THz for B2 and 5.3 THz for B3, by acquiring the beam patterns in amplitude in multiple planes using a heterodyne technique. The measured results show small deviations in both parameters relative to the simulations. Lastly, we also performed a qualitative verification of the beam pattern by scanning it over a large area for the B2 lens. The measured beam has good agreement with the simulations for the beam orientation, sidelobe shape, and location. Our experimental results verify the accuracy of the simulations. Therefore, our work has delivered the mixers with the required beam characteristics for a practical heterodyne instrument, GUSTO.

APPENDIX A
SIMULATIONS

A. HFSS Simulations

Fig. 11 shows the HFSS input structure used in our simulations. The antenna is located in a plane between two homogeneous media, vacuum ($\varepsilon = 1$) and Silicon ($\varepsilon_{Si} = 11.4$). The HEB is replaced by an excitation port centered on the antenna feed.

The antenna structure is set as a perfectly conducting surface. The boundary surfaces, outer surfaces of the Si and vacuum hemisphere in Fig. 11, are set as "radiation boundary" and have a radius of 300 μm. The "Global Material Environment" was set to Silicon. The antenna's far-field beam patterns into the Si medium were simulated at five different frequencies of 1.4, 1.9, 2.5, 4.7, and 5.3 THz, respectively. For the simulations, we obtained a $S_{11} \approx -12$ dB.

B. Geometrical and PO

The simulation of the integrated lens-antenna system in HFSS is not practical because it requires enormous computation power due to the large lens dimensions, e.g., 10 mm diameter, in comparison with the small wavelength of the supra-THz radiation. Therefore, we have split the simulations into multiple steps, namely first simulating the far-field beam pattern of the antenna in the homogeneous Si medium, mapping the radiation of the antenna on the surface of the lens using GO, and then calculating the far-field beam pattern using PO. We apply this mixed approach to compute the far-field beam pattern of our lens-antenna system in the desired plane.

Fig. 12 presents a schematic of the model used to simulate the far-field beam pattern in a given XY plane along the Z-axis. Let the electric field distribution of the antenna's far-field radiation be $U(P_0)$. To calculate the field distribution $U(P_1)$ in the plane of interest we integrate the PO Fresnel Kirchhoff diffraction formula [36] in (A.1). This assumes geometric mapping of the far field antenna beam pattern on the lens surface, S_1, which in our case is valid since the lens surface is in the far field of the antenna.

$$U(P_1) = \cdots$$
$$\frac{i}{2\lambda} \int \int_S U(P_0) \cdot \frac{\exp(ik(r+s))}{rs}$$
$$\cdot \left[\cos\left(\vec{n}, \vec{r}\right) + \cos\left(\vec{n}, \vec{s}\right) \right] dS_1. \quad (A.1)$$

Here, λ is the wavelength. k is the wavenumber $2\pi/\lambda$. S_1 is elliptical lens surface. $\vec{r}$ is the vector from P_0 to a point in the surface S_1 and r the respective length. $\vec{s}$ is the vector from a

point in the surface S_1 to P_1 and s the respective length. $\vec{n}$ is the normal vector to the surface S_1.

The intensity (I) is calculated using the following equation:

$$I\left(P_1\right) = \left|U\left(P_1\right)\right|^2. \tag{A.2}$$

APPENDIX B
GAUSSIAN BEAM ANALYSIS

For all the cases described in this work, the far-field radiation patterns were calculated in three different far-field planes. The calculated beams are fitted by a general 2-D Gaussian profile:

$$I = A \cdot \exp\left(-2\left(\frac{x^2}{w_x^2} + \frac{y^2}{w_y^2}\right)\right). \tag{B.1}$$

Here, x and y define two orthogonal axes for the beam, with w_x and w_y the beam radius dimension along the respective axis in a particular plane. Because our measurements, see Section IV, are in amplitude only, and because all the beams considered in this article are in the far field, our simulation analysis will be done using the beams in amplitude only, for consistency. After calculating w_x and w_y for each plane we fit the beam propagation in (B.2) [37] to obtain the beam waist radius, w_{0x} and w_{0y}, and Z_0

$$w\left(z\right) = w_0\sqrt{1 + \left(\frac{Z - Z_0}{Z_C}\right)^2} \tag{B.2a}$$

$$Z_C = \frac{\pi w_0^2}{\lambda}. \tag{B.2b}$$

Z is the distance between the antenna and the plane where the beam is computed. The value of Z_0 is defined relative to the antenna position. Positive Z_0 locations are in the direction of the lens. The antenna position is always located at the back surface of the simulated lens. Z_C is the confocal distance. Despite the beams showing astigmatism, i.e., different Z_{0x} and Z_{0y}, associated with beam ellipticity, we found the variation between both phase centers to be at least a factor of 3 below Z_C. Therefore, for simplification, in all our analysis we assume both orthogonal directions to have the same Z_0. With this simplification, we have less than 1% coupling loss error. Another simplification in our analysis is the final w_0 output, which is the average between w_{0x} and w_{0y}.

REFERENCES

[1] C. K. Walker, "THz coherent detection systems," in *Terahertz Astronomy*, 1st ed. New York, NY, USA: Taylor & Francis, 2016, pp. 159–227.

[2] C. Pabst et al., "Disruption of the Orion molecular core 1 by wind from the massive star θ^1 Orionis C," *Nature*, vol. 565, no. 7741, pp. 618–621, 2019.

[3] Y. M. Seo et al., "Probing ISM structure in Trumpler 14 and carina I using the stratospheric terahertz observatory 2," *Astrophys. J.*, vol. 878, no. 2, 2019.

[4] K. Tadaki et al., "The gravitationally unstable gas disk of a starbust galaxy 12 billion years ago," *Nature*, vol. 560, no. 7720, pp. 613–616, 2018.

[5] R. Güsten et al., "Disruption of the Orion molecular core 1 by wind from the massive star θ^1 Orionis C," *Nature*, vol. 56, pp. 357–359, 2019.

[6] The Event Horizon Telescope Collaboration, "First M87 event horizon telescope results. I. The shadow of the supermassive black hole," *Astrophys. J. Lett.*, vol. 875, no. 1, 2019.

[7] H. Linz et al., "Bringing high spatial resolution to the far-infrared," *Exp. Astron.*, vol. 51, 2021, Art. no. 661.

[8] E. Novoselov and S. Cherednichenko, "Low noise terahertz MgB$_2$ hot-electron bolometer mixers with an 11 GHz bandwidth," *Appl. Phys. Lett.*, vol. 110, 2017, Art. no. 032601.

[9] W. Zhang et al., "Quantum noise in a terahertz hot electron bolometer mixer," *Appl. Phys. Lett.*, vol. 96, no. 11, pp. 11–13, 2010.

[10] J. V. Siles et al., "Development of high-power multi-pixel LO sources at 1.47 THz and 1.9 THz for astrophysics: Present and future," in *Proc. 26th Int. Symp. Space Terahertz Technol.*, 2015, pp. 40–42.

[11] B. S. Williams, "Terahertz quantum-cascade lasers," *Nature Photon.*, vol. 1, pp. 517–525, 2007.

[12] A. Khalatpour et al., "A tunable unidirectional source for GUSTO's local oscillator at 4.74 THz," *IEEE Trans. THz Sci. Technol.*, vol. 12, no. 2, pp. 144–150, Mar. 2022.

[13] P. Putz et al., "HEB waveguide mixers for the upGREAT 4.7 THz heterodyne receiver array," in *Proc. 27th Int. Symp. Space THz Technol.*, 2016, pp. 27–29.

[14] W. Zhang et al., "Noise temperature and beam pattern of an NbN hot electron bolometer mixer at 5.25 THz," *J. Appl. Phys.*, vol. 108, 2010, Art. no. 093102.

[15] J. R. Gaspar Silva et al., "High accuracy pointing for quasi-optical THz mixer arrays," *IEEE Trans. THz Sci. Technol.*, vol. 12, no. 1, pp. 53–62, Jan. 2022.

[16] J. Dyson, "The equiangular spiral antenna," *IRE Trans. Antennas Propag.*, vol. 7, no. 2, pp. 181–187, Apr. 1959.

[17] P. Khosropanah, J. R. Gao, W. M. Laauwen, and M. Hajenius, "Low noise NBN hot electron bolometer mixer at 4.3 THz," *Appl. Phys. Lett.*, vol. 91, 2007, Art. no. 221111.

[18] D. F. Filipovic, S. S. Geahart, and G. M. Rebeiz, "Double-slot antennas on extended hemispherical and elliptical silicon dielectric lenses," *IEEE Trans. Microw. Theory Techn.*, vol. 41, no. 10, pp. 1738–1749, Oct. 1993.

[19] A. D. Semenov et al., "THz performance of integrated lens antennas with a hot-electron bolometer," *IEEE Trans. Microw. Theory Techn.*, vol. 55, no. 2, pp. 239–247, Feb. 2007.

[20] W. Zhang et al., "Twin-slot antenna coupled NbN hot electron bolometer mixer at 2.5 THz," *IEEE Trans. THz Sci. Technol.*, vol. 1, no. 2, pp. 378–382, Nov. 2011.

[21] B. D. Jackson, "NbTiN-based THz SIS mixers for the Herschel space observatory," Ph.D. dissertation, Fac. Appl. Sci., TU Delft, Delft The Netherlands, 2005.

[22] C. Walker et al., "Gal/xgal U/LDB spectroscopic/stratospheric THz observatory: GUSTO," *Proc. SPIE*, vol. 12190, 2022, Art. no. 121900E.

[23] J. R. Gaspar Silva et al., "4×2 HEB receiver at 4.7 THz for GUSTO," *Proc. SPIE*, vol. 10708, 2018, Art. no. 107080Z.

[24] M. Van Der Vorst, "Integrated lens antennas for submillimetre-wave applications," Ph.D. dissertation, TU Eindhoven, Eindhoven, The Netherlands, 1999.

[25] W. Jellema, "Optical design and performance verification of Herschel-HIFI," Ph.D. dissertation, Univ. Groningen, Groningen, The Netherlands, 2015.

[26] A. Garufo, N. Llombart, and A. Neto, "Radiation of logarithmic spiral antennas in the presence of dense dielectric lenses," *IEEE Trans. Antennas Propag.*, vol. 64, no. 10, pp. 4168–4177, Oct. 2016.

[27] W. Miao et al., "Simulation of an integrated log-spiral antenna at terahertz," in *Proc. IEEE 8th Int. Symp. Antennas, Propag. EM Theory*, 2008, pp. 58–61.

[28] W. Jellema et al., "Phase-sensitive near-field measurements and electromagnetic simulations of a double-slot HEB integrated lens-antenna mixer at 1.1, 1.2 and 1.6 THz," in *Proc. 16th Int. Symp. Space THz Technol.*, May 2005, pp. 399–404.

[29] J. R. Gaspar Silva et al., "Preliminary design study of a 4×2 HEB array at 4.7 THz for GUSTO," in *Proc. 29th Int. Symp. Space THz Technol.*, 2018, pp. 82–86.

[30] HFSS. [Online]. Available: www.ansys.com

[31] Sumipro – Optical solutions. [Online]. Available: www.sumipro.nl

[32] J. Kaiser, "The Archimedean two-wire spiral antenna," *IRE Trans. Antennas Propag.*, vol. 8, pp. 312–323, May 1960.

[33] J. R. Gaspar Silva et al., "High accuracy pointing for quasi-optical THz mixer arrays," *IEEE Trans. THz Sci. Technol.*, vol. 12, no. 1, pp. 53–62, Jan. 2022.

[34] S. Hähnle et al., "An ultrawideband leaky lens antenna for broadband spectroscopic imaging applications," *IEEE Trans. Antennas Propag.*, vol. 68, no. 7, pp. 5675–5679, Jul. 2020.

[35] The FIR gas laser is known to be sensitive to the environment, such as the temperature etc, so it is difficult to keep it stable for long periods of time. This limits the continuous scanning for a long period, e.g., one hour, at the lower frequencies.

[36] E. Wolf and M. Born, "Elements of the theory of diffraction," in *Principles of Optics: Electromagnetic Theory of Propagation, Interference and Diffraction of Light*, 7th ed., Cambridge, U.K.: Cambridge Univ. Press, 1999.

[37] P. F. Goldsmith, "Gaussian beam propagation," in *Quasioptical Systems: Gaussian Beam Quasioptical Propagation and Applications*. Piscataway, NJ, USA: IEEE Press, 1998, pp. 9–38.